ELECTRONIC SUPPLEMENTARY INFORMATION to

Controlled dynamics of a Vanadyl-based qudit with remarkable coherence

S. Chicco,[1,2] A. Chiesa,[1,2] G. Allodi,[1,2] E. Garlatti,[1,2] M. Atzori,[3] L. Sorace,[3] R. De Renzi,[1] R. Sessoli,[3] and S. Carretta[1,2]

[1] *Università di Parma, Dipartimento di Scienze Matematiche, Fisiche e Informatiche, I-43124 Parma, Italy*

[2] *UdR Parma, INSTM, I-43124 Parma, Italy*

[3] *Dipartimento di Chimica "Ugo Schiff" INSTM, Università Degli Studi di Firenze, I-50019 Sesto Fiorentino, Italy*

(Dated: July 21, 2021)

I. SYNTHESIS AND CHARACTERIZATION

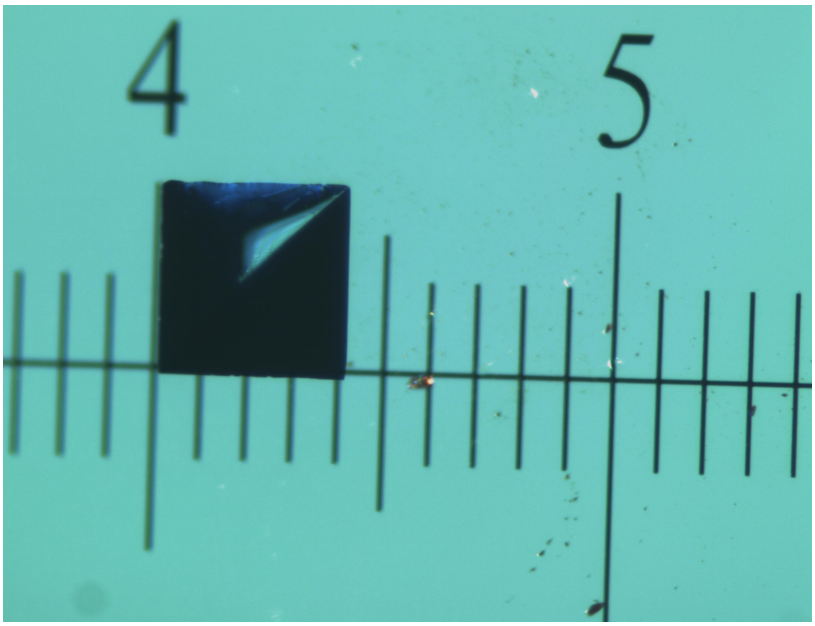

FIG. 1. Photograph of a single crystal of [VO(TPP)] used for NMR measurements, showing crystal dimentions and the characteristic square pyramid shape with ab-plane as its base and c-axis as its height.

II. EXPERIMENTAL DETAILS

A. NMR spectrometer

The unconventional NMR spin-echo measurements are carried out by means of a home-built broadband and phase-coherent NMR spectrometer 'HyReSpect' [1]. The sample environment consist in a Maglab EXA (Oxford Instruments) 0-9 T superconducting magnet equipped with a helium flow insert, ensuring homogeneity of the applied magnetic field and temperature stability. This 'HyReSpect' spectrometer is particularly suitable to excite and detect the short and fast decaying echoes characterizing the present experiment. This is granted by a flat response over a wide frequency span $8 - 8000$ MHz, and by the ability to target the sample with short rectangular pulses ($P_{\frac{\pi}{2}} \approx 200$ ns in this experiments). The radio frequency (rf) pulses are amplified by a linear pulse power amplifier and fed into the NMR probehead. The probehead, hosted by the cryostat, consists in a LC resonant circuit,

made of a small coil ($\sim$ 300 nH) which is wound around a non-magnetic plastic crystal holder, and a Voltronics NTNM-120 variable capacitor, providing a wide tuning range. In low temperature regimes, the Q-factor of the resonant probehead in the used configuration, is in the order of 200. Automated frequency scans are allowed by the employment of a servo-assisted automatic probe tuning system.

B. Hahn-echo sequences

The pulse sequence adopted for the echoes excitation and detection of NMR spectra consists of two equal rf pulses ($T_{pulse} = 0.202\,\mu$s, $T_{echo} = 0.202\,\mu$s), with rf power optimized for the maximum resonance signals, separated by a delay $\tau \approx 6\,\mu$s. Such a condition corresponds to a $\frac{2\pi}{3}$ nutation angle ($\frac{2\pi}{3} - \tau - \frac{2\pi}{3}$ sequence) [2]. The choice of this sequence, (characterized by a $\frac{2\pi}{3}$ in place of the standard π refocusing pulse), is justified by the better tolerance to non optimal pulse calibration (e.g. imperfect rf power) and by the shorter overall duration of the sequence, advantageous for short-T_2 systems and for the more efficient refocusing of broad spectral lines.

C. NMR Spectra

NMR spectra are collected for both crystallographic inequivalent directions (ab plane, c axis) by recording echoes at variable frequency with relative steps of 0.8 MHz (see fig. 2). In our experiment, the instrumental parameters are varied to optimize the transition detection for each spectral region at each applied field. As a consequence the transition intensities, which strongly depend on the experimental setup, e.g. the linear response of power amplifier, are not considered as a crucial parameter for the system characterization.

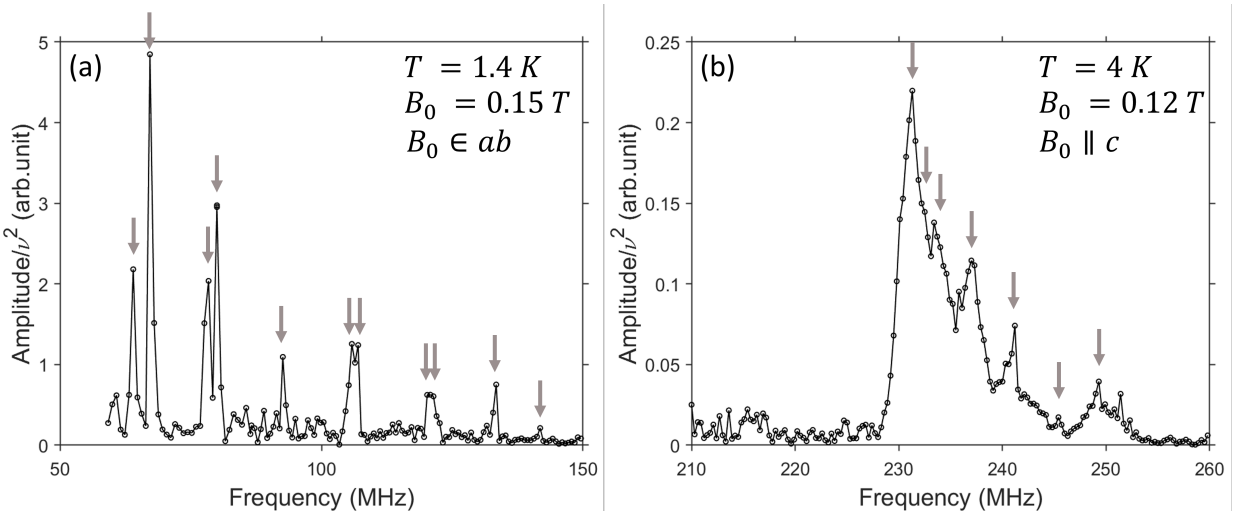

FIG. 2. Two example of NMR spectra are shown: on the left, the field $B_0 = 0.15$ T is applied in the abplane at $T = 1.4$ K; On the right, the field $B_0 = 0.15$ T is applied along the c axis of the molecule (see main text) at $T = 4$ K.

D. Nuclear eigenstates

The energy level diagram of the coupled electro-nuclear system (calculated by diagonalization of the spin Hamiltonian with parameters fitted from NMR spectra) is reported in Fig. 3 below, with the field applied both in ab plane and along c axis. For this latter orientation the electronic and nuclear components of the eigenstates are already factorized at lower magnetic field, due to the smaller values of $A_{x,y}$ compared to A_z. At the same time, this reduced electro-nuclear mixing makes different nuclear transitions closer in frequency (i.e. it yields a smaller effective quadrupole) as evidenced by the equal spacing of nuclear levels in the close-up of 3-(e,f), thus making it difficult to separately address each of them. This justifies our choice to focus most of our measurements and of the discussion in the main text on the ab orientation.

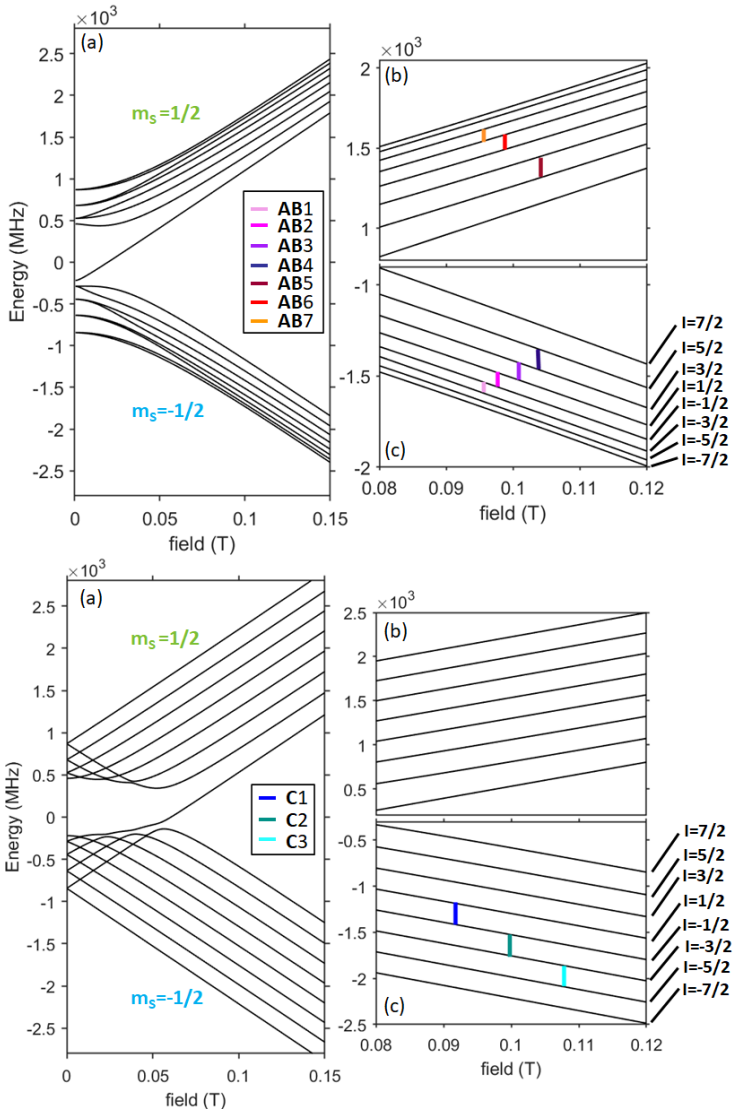

FIG. 3. Energy level diagram as a function of the static field, applied in the ab-plane (panel a,b,c) and along the c-axis (panel d,e,f). In the right panels (b,c,e,f), a close up of the nuclear levels within the electronic spin multiplets. The lowest manifold are labelled with the corresponding nuclear spin component along the field m_I .Coloured marks indicate nuclear transitions for which the nuclear spin dephasing T_2 is measured

E. Nuclear Spin dephasing times

Nuclear spin dephasing times are measured in both crystal directions, by exciting echoes with the same pulse sequence described above, varying the delay τ between exciting and refocusing pulses. The echoes intensity thus represent the precessing (resonant) component of

the transverse magnetization. For all investigated transitions (marked in the level diagrams of Fig. 3) the echoe decays are well modeled by a single exponential decay as a function of τ.

$$M(\tau) = M_0 e^{-\frac{2\tau}{T_2}}$$

where T_2 represents the decoherence time related to the levels specifically involved in the transition. In the following we report examples of this single exponential decay (figure 4-(a,b)), and the measured T_2 as a function of the applied field (figure 4(c,d) for both the crystallographic direction studied. The T_2 values obtained are found to be comparable between the two directions.

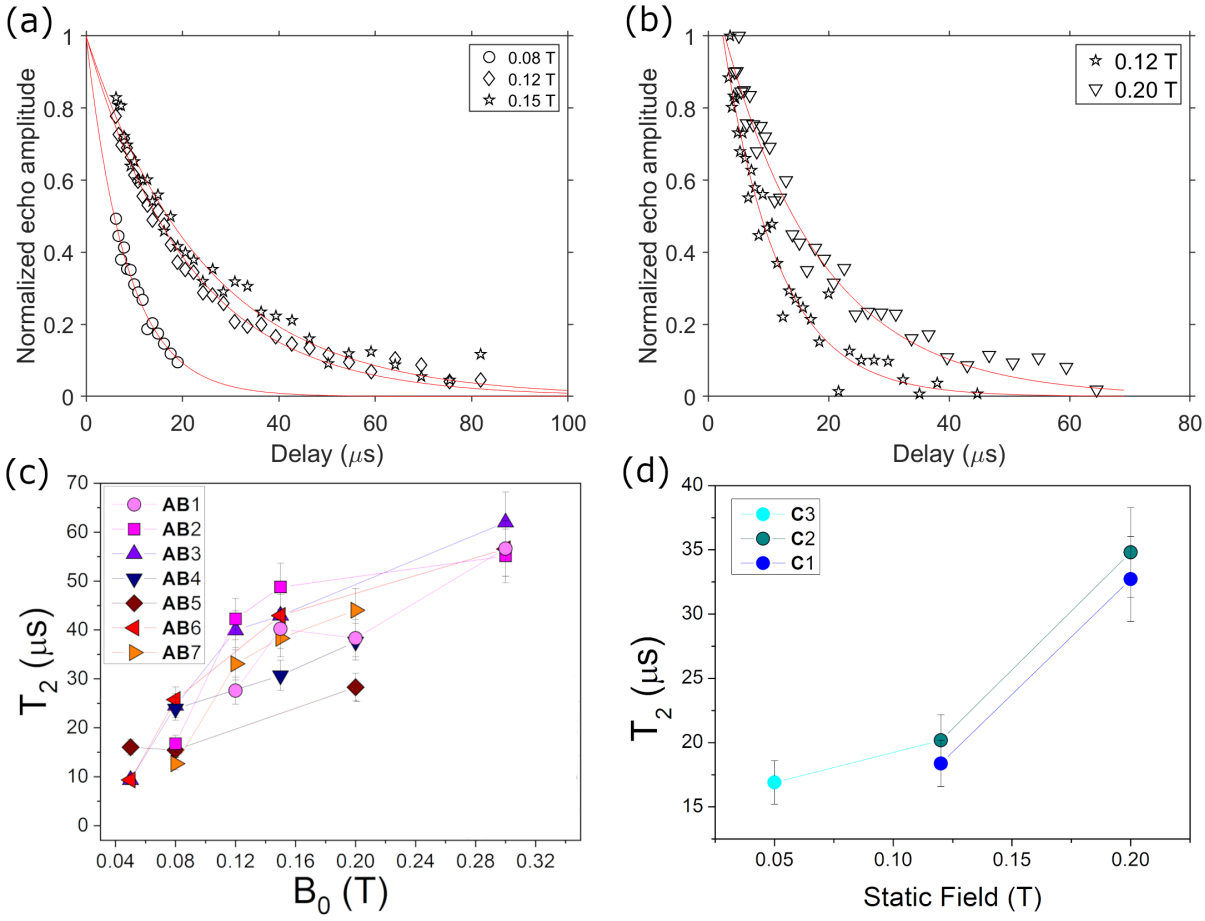

FIG. 4. Nuclear spin relaxation experiments, performed in both the crystal direction of interest: *ab*-plane and *c*-axis. In panels (a) and (b) we show the single exponential decay of the transverse magnetization for static field B_0 applied in the *ab*-plane and along the *c*-axis respectively, while in panels (c,d) the measured T2 as a function of that field for both directions.

F. Rabi Nutation experiments

As described in the main text, Rabi oscillations are induced on the nuclear spin system to demonstrate the capability to individually address and manipulate nuclear state. The pulse sequence differs from the one used to excite spectra, since the first pulse of variable length induces a $\theta(t)$ nutation of the spin system in the rotating frame, and the refocusing is generated by a π-pulse.

Regarding the signal detection procedure, the effective bandwidth of the experiment is determined by the finite value of the radio frequency field B_1 (whereby only frequency component such that $\Delta\omega < \gamma B_1$ are effectively excited), the finite bandwidth of the spectrometer (± 3 MHz) and the Q-factor of the LC probehead. The overall transfer function is the product of the three terms above, which yields an overall bandwidth in the order of ± 1 MHz. This prevents the simultaneous excitation and detection of adjacent transitions. Hence, the simulation of the time evolution of the system is fundamental to demonstrate that we observe monochromatic Rabi oscillations.

The decay of Rabi oscillation intensities, at which contribute T_2 and the inhomogeneity of the oscillating field B_1, is dominated by the latter as evidenced in figure 5.

As stated in the main text, the Rabi frequencies is a linear function of the exciting amplitude

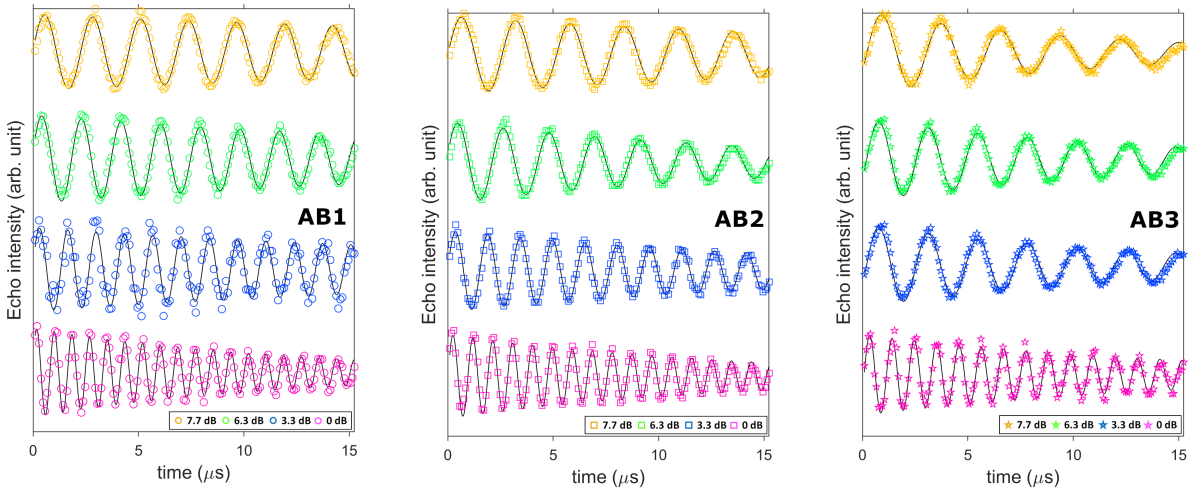

FIG. 5. Rabi oscillations induced on transitions **AB**1,2,3 with the static field along $\hat{\boldsymbol{x}}$ and the oscillating pulse along $\hat{\boldsymbol{z}}$, for different applied rf power.

(figure 6), indicating that the observed oscillations are induced by the pulse.

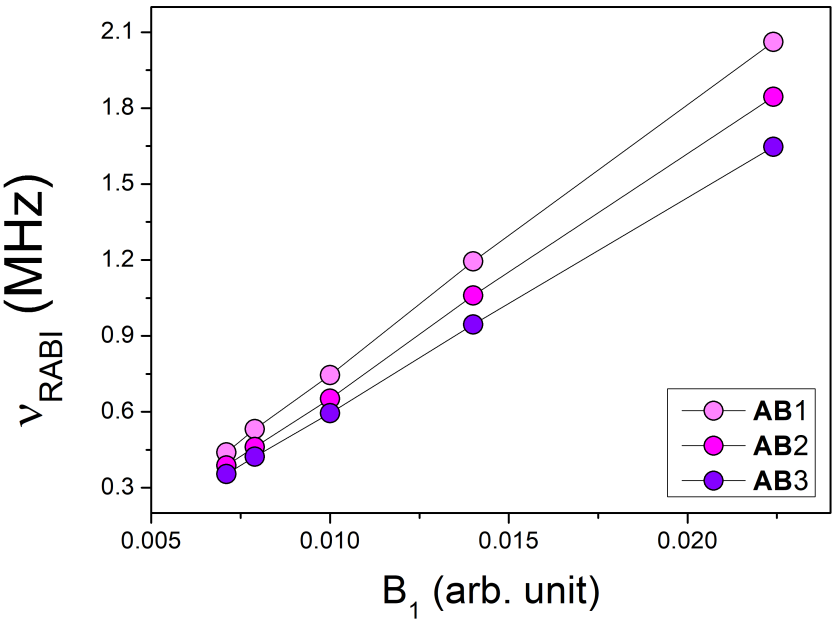

FIG. 6. Rabi frequency dependence on the applied rf field B_1 for transitions **AB**1,2,3.

III. SIMULATIONS OF NUCLEAR SPIN TRANSITIONS

To better investigate the time evolution of the nuclear states when targeted by a resonant pulse and to compare the results with the experiments, we numerically solve the Lindblad equation (see main text) for the system density matrix. We evaluate the effect of resonant pulses on pure (initialized in a given m_I, m_S state) or thermally populated states, matching in the latter case the experimental conditions, $T = 1.4$ K. At this temperature, all the nuclear eigenstates are populated, within both the electronic spin multiplets (see figure 3). Instead, a condition in which only the $m_S = -\frac{1}{2}$ manifold is populated, can be reached by working at $T < 100$ mK (as routinely done in many quantum-computing platforms, see e.g. [3]) or by exploiting algorithmic cooling methods, see e.g. [4].

Simulations are performed at the applied static field of $B_0 = 0.3$ T, and with a radiofrequency exciting pulse on transitions **AB** 1,2,3. The chosen experimental conditions represent a good trade off between electro-nuclear entanglement and spectral separation, as described in the main text. The excitations are made by addressing the state with a linearly polarized rectangular pulse of amplitude $B_1 \approx 5$ G, which matches the experimental scenario and gives a negligible leakage to neighboring levels. We found that only the levels targeted by the resonant pulse undergo significant population changing, as shown in figures 7 and 8 for an initialized and a thermal populated initial state, respectively. We can see that the target state evolves correctly from $m_I = -3/2$ to $m_I = -1/2$ [Fig. 7-(c), 8-(c)], from $m_I = -1/2$ to $m_I = 1/2$ [Fig. 7-(b), 8-(b)] and from $m_I = 1/2$ to $m_I = 3/2$ [Fig. 7-(a), 8-(a)].

At the experimentally probed temperature (1.4 K), also states belonging to the $m_S = \frac{1}{2}$ multiplet are populated. However, we find that only a few of them are close to resonance and hence slightly affected by the pulse and the corresponding variation of population in the time-scale of a full Rabi-flop is much smaller than those on the targeted pair of levels [see Fig 8, panels (g,h,i)]. This does not occur when the system is prepared in a specific initial state.

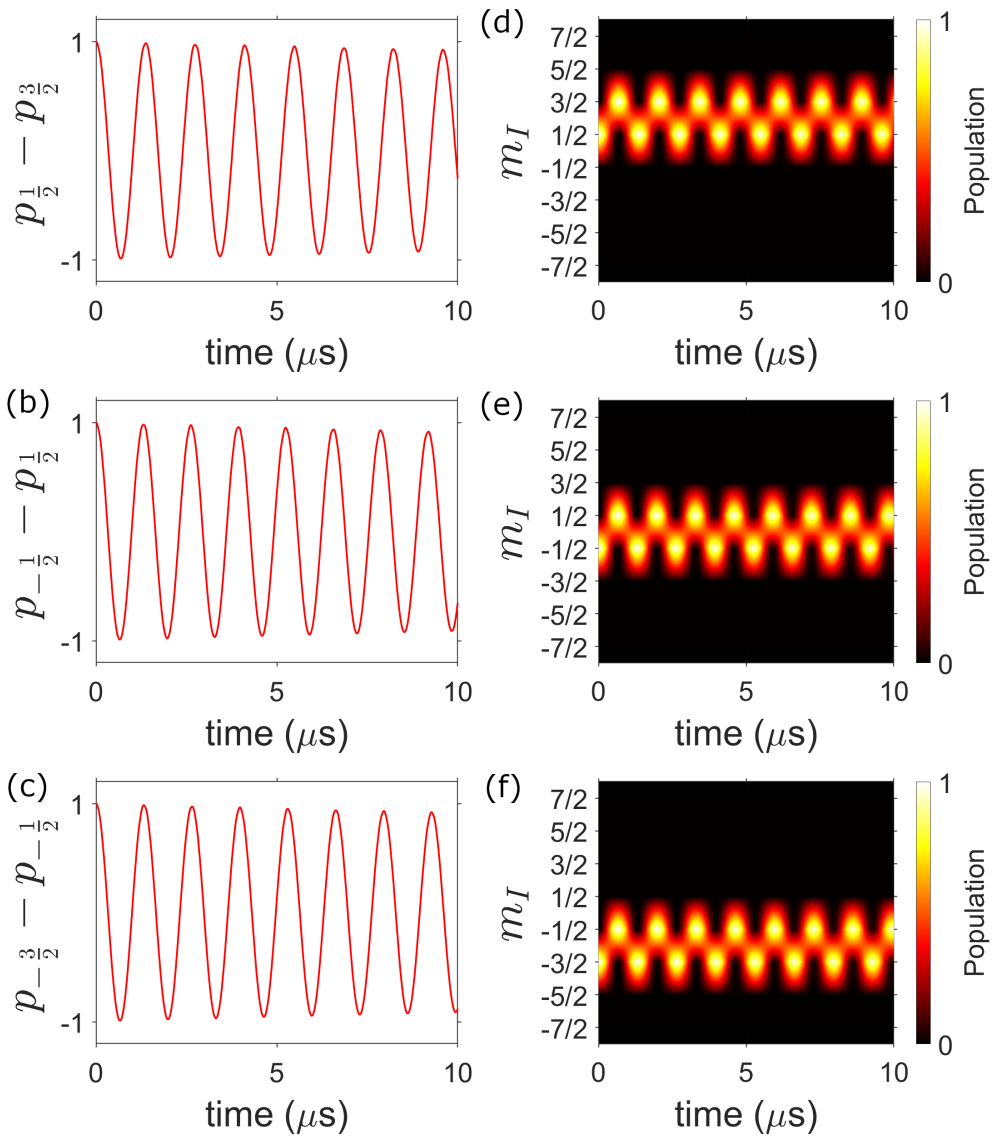

FIG. 7. Simulated time evolution of the population of the different nuclear spin levels, within $m_S = -1/2$ subspace. The static field is applied along x and quantum numbers m_I, m_S are eigenvalues of I_x, S_x. The system is prepared in specific initial states $m_I = -3/2, -1/2, 1/2$ and addressed by an oscillating field resonant with specific $\Delta m_I = 1$ transitions: (a,d) $m_I = -3/2 \rightarrow -1/2$, (b,e) $m_I = -1/2 \rightarrow 1/2$, (c,f) $m_I = 1/2 \rightarrow 3/2$. Left panels (a-c): difference between population of the two addressed levels. Right (d-f): 2D heat-maps of the population fraction for each nuclear level, showing that only the targeted levels exhibit sizable oscillations, while leakage to other levels is negligible ~ 0. Several Rabi oscillations are shown, including the effect of pure dephasing with the measured values of $T_2^{m_I,m_I'}$.

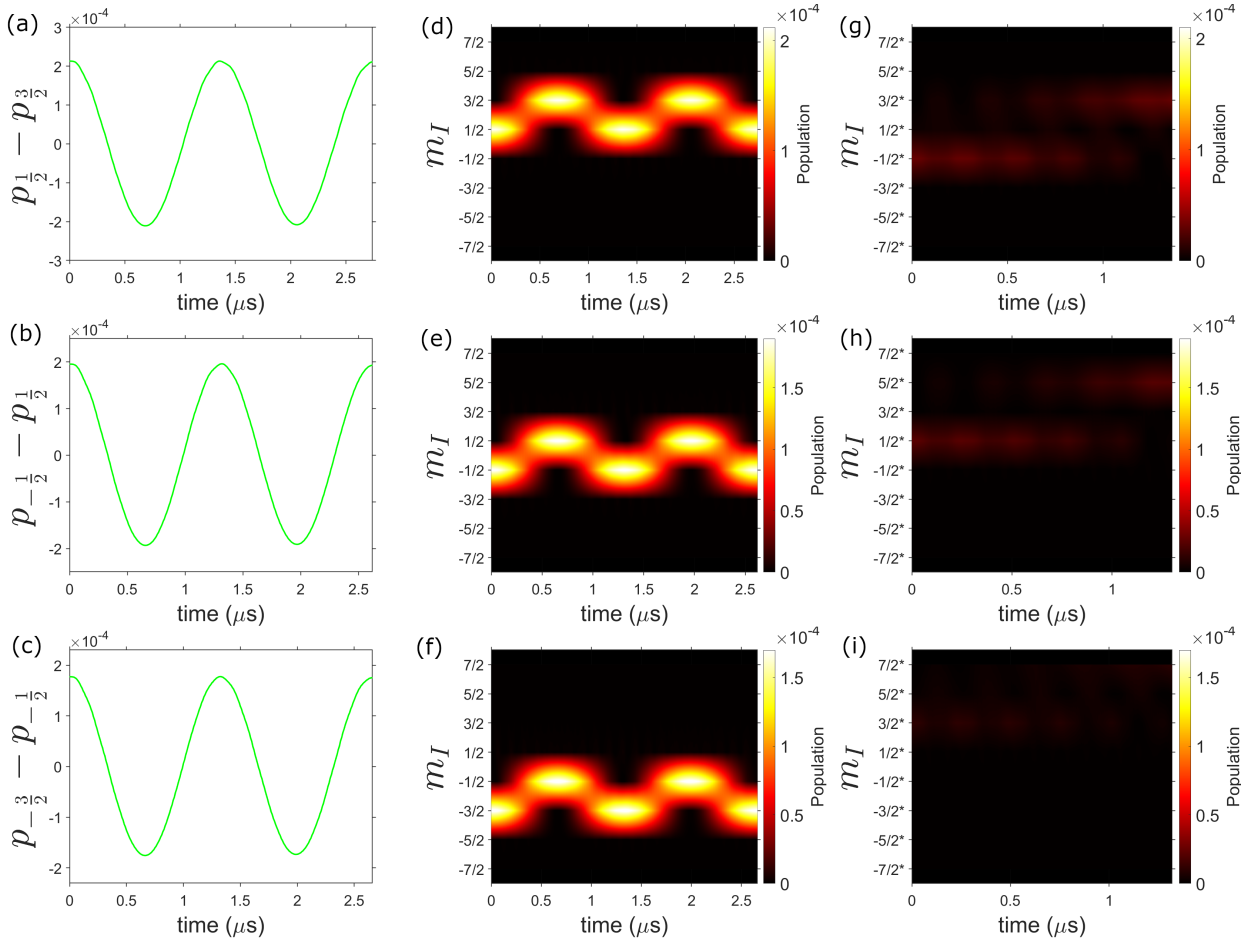

FIG. 8. Time evolution of the population of the different nuclear spin levels, with initial thermal density matrix $\rho = \sum_k p_k |k\rangle\langle k|$ and $p_k = exp(-E_k/k_B T)/Z$, with k labelling the eigenstates when m_I does not represent a good quantum number. The system is prepared at $T = 1.4$ K, thus with both the $m_S = \pm 1/2$ subspaces populated, and addressed by an oscillating field resonant with the same specific $\Delta m_I = 1$ transitions of figure 7. Left panels (a-c): difference between population of the two addressed levels. Central (d-f) and Right (g-i): 2D heat-maps of the population variation for each nuclear level within the $m_S = -1/2$ and $m_S = 1/2$ subspaces respectively.

[1] G. Allodi, A. Banderini, R. D. Renzi, and C. Vignali, Hyrespect: A broadband fast-averaging spectrometer for nuclear magnetic resonance of magnetic materials, Rev. Sci. Instrum. **76**, 083911 (2005).

[2] E. L. Hahn, Spin echoes, Phys. Rev. **80**, 580 (1950).

[3] G. Wendin, Quantum information processing with superconducting circuits: a review, Rep. Prog. Phys. **80**, 106001 (2017).

[4] D. K. Park, G. Feng, R. Rahimi, S. Labruyère, T. Shibata, S. Nakazawa, K. Sato, T. Takui, R. Laflamme, and Baugh, Hyperfine spin qubits in irradiated malonic acid: heat-bath algorithmic cooling, J. Quantum Inf. Process **14**, 2435 (2015).